Materials Science and Engineering B 324 (2026) 118949

Contents lists available at ScienceDirect

Materials Science & Engineering B

journal homepage: www.elsevier.com/locate/mseb

Hydrothermal synthesis of hollow Fe_2O_3 microspheres: effect and mechanism of glucose concentration

Hong Yin [a], Linfei Yu [a], Jiahui Zheng [a], Chenliang Zhou [a,*], Wenxiu He [a], Gewen Yu [a], Jian Ding [a], Qiang Zhang [b], Quansheng Liu [c]

[a] Inner Mongolia Key Laboratory of Coal Chemical Industry and Comprehensive Utilization, Inner Mongolia University of Science & Technology, Baotou 014010, China
[b] Inner Mongolia Western Region New Energy Development Group Co., Ltd., Baotou 014010, China
[c] Inner Mongolia Key Laboratory of High-Value Function Utilization of Low Rank Carbon Resource, Inner Mongolia University of Technology, Hohhot 010051, China

ARTICLE INFO

Keywords:
Glucose concentration
Hollow Fe_2O_3 microspheres
Reaction mechanism

ABSTRACT

Hollow Fe_2O_3 microspheres were synthesized via a hydrothermal method using ferric nitrate nonahydrate ($Fe(NO_3)_3{\cdot}9H_2O$), anhydrous glucose and deionized water as iron source, shape directing agent and solvent, respectively. The structure, morphology, grain size and crystal phase of hollow Fe_2O_3 were characterized using X-ray Diffraction (XRD), X-ray photoelectron spectroscopy (XPS), Scanning Electron Microscopy (SEM), Brunauer-Emmett-Teller (BET) analysis, Thermogravimetry-Differential Thermal Analysis (TG-DTA) and Fourier Transform Infrared Spectroscopy (FTIR). Research indicates that by regulating glucose concentration, the formation mechanisms of different morphologies of Fe_2O_3 can be controlled. At a concentration of 0.45 mol/L and hydrothermal reaction temperature is 180 °C, hollow Fe_2O_3 (Fe-0.45) is formed with an average particle size of 2.99 μm, average pore diameter of 20.3 nm, and specific surface area of 20.1 m^2/g. During the reaction process, the organic acids generated from glucose oxidation combine with Fe^{3+} or Fe^{2+} (reduced from Fe^{3+}) to form metal-organic intermediate phases, which thermodynamically evolve to ultimately produce single α-phase crystals. This results in a hollow mesoporous framework encapsulated by aggregated nanoparticle shells, exhibiting high thermal stability and multifunctional properties.

1. Introduction

In the realm of materials science, the development of advanced functional materials has garnered significant attention due to their wide-ranging applications in various fields such as electronics, energy and environmental protection. Among these, superhydrophobic coatings have emerged as a promising class of materials with potential applications in self-cleaning surfaces, anti-corrosion, and anti-icing [1,2]. The unique properties of superhydrophobic coatings stem from their ability to repel water, which is attributed to the combined effects of surface chemistry and micro/nano-structures [3,4]. In this context, hollow microspheres of iron oxide (Fe_2O_3) have shown great potential as building blocks for superhydrophobic coatings. They can not only serve as microscale materials but also act as protective "armor" for nanoscale materials to enhance the wear resistance and hydrophobicity of coatings as shown in Fig. 1 [5].

Iron oxide(Fe_2O_3), commonly known as hematite, is a widely studied material due to its abundance, low cost and non-toxicity [8]. It possesses excellent chemical stability, mechanical strength and optical properties, making it a suitable candidate for various applications. The hollow structure of Fe_2O_3 microspheres offers several advantages [9]. Firstly, the hollow interior can reduce the density of the material, which is beneficial for lightweight applications. Secondly, the thin shell of the hollow microspheres provides a large surface area, which can offer more grafting sites for hydrophobic groups, thereby enhancing the repulsion against water molecules and contributing to the improvement of superhydrophobic performance. Moreover, the hollow structure can act as a buffer to protect the core material from external environmental factors, thereby improving the durability of the superhydrophobic coatings.

Despite the promising potential of Fe_2O_3 hollow microspheres, their preparation remains a challenging task. Traditional methods for synthesizing hollow structures often involve complex procedures, high temperatures or the use of toxic chemicals, which can limit their large-scale production and practical applications. Therefore, there is a need to develop a simple, cost-effective, and environmentally friendly method

* Corresponding author.
E-mail address: zhouchenliang@imust.edu.cn (C. Zhou).

https://doi.org/10.1016/j.mseb.2025.118949
Received 24 August 2025; Received in revised form 18 October 2025; Accepted 25 October 2025

for the synthesis of Fe_2O_3 hollow microspheres.

To date, Fe_2O_3 hollow microspheres has been synthesized using various methods, including hydrothermal synthesis [10], sol-gel method [11] and electrospinning [12]. The hydrothermal method, known for its low cost, simple process and lack of complex equipment requirements [13], is preferred for synthesizing Fe_2O_3 hollow microspheres. For instance, Hossain et al. [10] synthesized hollow α-Fe_2O_3 using fructose and anhydrous ferric chloride as precursors. Which maintains structural stability even at 700 °C, demonstrating excellent thermal stability. Zhang et al. [14] and Kang et al. [15] demonstrated that glucose concentration significantly influences material morphology in hydrothermal systems, confirming that synthesis conditions, particularly glucose concentration, are critical factors for controlling the structure of hollow α-Fe_2O_3.

In this study, the nitrate ions in the hydrothermal solution react with glucose through oxidation/carbonization processes as shown in Fig. 2, generating a series of intermediate products and carbon templates (oxidation/carbonization–coordination reaction mechanism). The intermediate products from oxidation serve to provide active sites for the reaction, facilitating the uniform dispersion of iron ions and regulating the reaction rate. Meanwhile, the carbon templates offer structural support, enhancing the stability of the reaction. Herein, with ferric nitrate as the precursor and its concentration kept constant to ensure a definite oxidation/carbonization capacity, the content of glucose is varied to alter the formation of intermediate products and carbon templates. This approach allows for the investigation of the influence of glucose concentration on the formation of Fe_2O_3 hollow microspheres, and aims to lay the foundation for the low-cost and highly controllable synthesis of Fe_2O_3 hollow microspheres.

2. Experimental section

2.1. Synthesis of hollow Fe_2O_3

$Fe(NO_3)_3{\cdot}9H_2O$, anhydrous glucose and deionized water were used as raw materials. All of the chemicals were purchased from Sinopharm Chemical Reagent Co., Ltd., without further purification. A mixture was prepared by dissolving 0.009 mol $Fe(NO_3)_3{\cdot}9H_2O$ and a precise quantity of anhydrous glucose in 100 mL of deionized water, and stirred to ensure uniform distribution. Then the mixture was transferred to the crystallization kettle and crystallized at 180 °C for 16 h. The resulting precipitate was washed and filtered to remove impurity ions and organic compounds. The product was subsequently dried in a drying oven for 12 h. Finally, calcine at 500 °C for 4 h. The samples before and after calcine were labeled as C-X and Fe-X respectively, where X represents the molar concentration of glucose in the solution, and X = 0 M, 0.09 M, 0.45 M, 0.9 M, 1.35 M and 1.8 M respectively. The process of sample preparation is illustrated in Fig. 3.

Transfer the 0.45 M glucose solution into Teflon-lined stainless-steel autoclave and heat them to 180 °C for 16 h. Following Fig. 3, wash the resulting product with water and ethanol, then dry it at 60 °C for an additional 12 h. The resulting samples were named CS.

2.2. Particle characterization

The morphology of the samples was analyzed using a scanning electron microscope (SEM, ZEISS Sigma 500). The crystal structure of the sample was characterized by X-ray diffraction (XRD, Bruker D8) and the diffraction angle 2θ ranged from 10 to 80°. The crystallite phase was estimated using the data from the Joint Committee on Powder Diffraction Standards (JCPDS). The average crystallite sizes of the hollow Fe_2O_3 were estimated by Scherrer's formula:

$$D = k\lambda/(\beta \cos\theta) \tag{1}$$

where $k = 0.9$ denotes the Scherrer constant, $\lambda = 0.154$ nm corresponds to the Cu Kα radiation wavelength, θ is the Bragg angle and β represents the Lorentzian-corrected full-width at half-maximum (FWHM) in radians.

To further investigate the microstructure changes of the samples after calcination, the Williamson-Hall (W—H) plot was used to fit the XRD of samples with different glucose concentrations. The calculation formula is as follows:

$$\beta cos\theta = \frac{k\lambda}{D} + 4\varepsilon sin\theta \tag{2}$$

where β represents the FWHM, θ is the Bragg angle, D is the average crystallite size, ε is the micro-strain, $k = 0.9$ and $\lambda = 0.154$ nm.

Thermal behavior of the precursor was characterized using thermogravimetric analysis (TG-DTA, STA2500) under an air atmosphere,

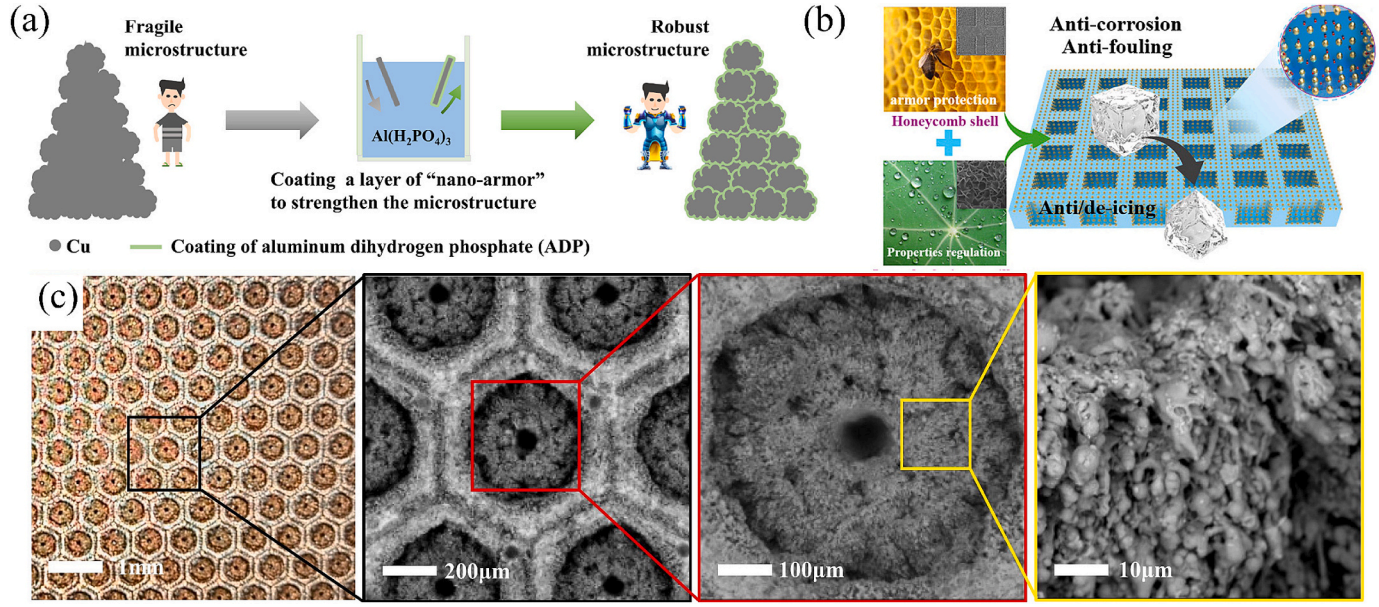

Fig. 1. (a) Schematic diagram of the concept of superhydrophobic materials for "nano armor" [5], (b) Superhydrophobic surface mimetic prototypes [6] and (c) Top-view SEM images of the honeycomb structure [7].

Fig. 2. Oxidation/carbonization processes

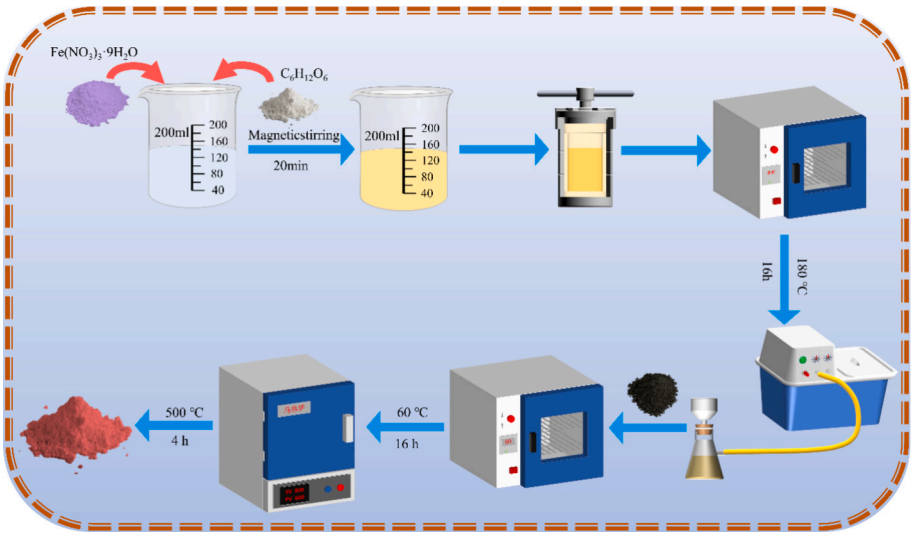

Fig. 3. Preparation process of hollow Fe_2O_3.

with a temperature range of 40–800 °C and a heating rate of 10 °C/min. The determination of functional groups in hollow Fe_2O_3 was carried out by Fourier transform infrared (FTIR, VERTEX 70, Bruker, Billerica, Massachusetts, USA) spectroscopy. The specific surface areas were measured via Brunauer-Emmett-Teller (BET , NOVA 1200e). The relevant components of Fe_2O_3 were detected by X-ray photoelectron spectroscopy (XPS) through measuring the electron binding energy (ESCALAB Xi+, Thermo Fisher Scientific, USA).

3. Results and discussion

3.1. XRD

XRD patterns of products before and after calcination are shown in Fig. 4. As depicted in Fig. 4(a), CS exhibit broad asymmetrical peak of carbon centered between 20 and 50°, which indicates that carbon has a combination of sp^2(26.6°, plane spacing d = 0.335 nm) and sp^3(43.9°, plane spacing d = 0.206 nm) lattice structures in the grains that combine to form the hollow spheres which have no long-range order [16]. The diffraction peaks of C-0.45, C-0.9, C-1.35 and C-1.8 at around 2θ = 18.7°, 19.0°, 23.0°, 29.8° and 46.8° are in good agreement with the reference data for the $FeC_2O_4·H_2O$ (PDF card number: 23–0239), corresponding to reflection planes of (200), (002), (−202), (202) and (402), respectively. This compound can be synthesized through the following reaction pathway: 1. During the hydrothermal treatment of glucose, a series of complex chemical reactions may lead to the formation of oxalic acid ($C_2H_2O_4$). In studies utilizing glucose under hydrothermal conditions, Ischia et al. [17] discovered the formation of intermediate products such as small carboxylic acids. Glucose exhibits reducing properties, capable of converting Fe^{3+} to Fe^{2+}, ultimately forming ferrous oxalate [18]. 2. In hydrothermal reactions, glucose may produce oxalic acid under the oxidative action of nitric acid, as shown in reaction Eq. (3) [19]. Glucose has reducing properties which allow it to convert Fe^{3+} to Fe^{2+}, resulting in the formation of ferrous oxalate [18]. As shown in Fig. 4(b), the diffraction peaks at 2θ = 24.1°, 33.1°, 35.6°, 40.8°, 49.4°, 54.1°, 57.5°, 62.4°, 64.0°, 72.0° and 75.5° are in good agreement with the reference data for the α-Fe_2O_3 (PDF card number: 33–0664), corresponding to reflection planes of (012), (104), (110), (113), (024), (116), (018), (214), (1010), (300) and (220), respectively. The absence of peaks for FeOOH, Fe_3O_4 and γ-Fe_2O_3 indicates that the product is pure α-Fe_2O_3 [20]. The transition from Fig. 4(a)–(b) demonstrates that the amorphous peak disappears after calcination and new XRD peaks emerge, indicating that the carbon-containing iron spheres undergo thermal decomposition of the carbon component during the calcination process, generating Fe_2O_3. During the hydrothermal reaction process, the absence of glucose leads to the direct hydrolysis or oxidation of iron precursors into thermodynamically more stable Fe_2O_3, rather than other intermediate states or complex structures. As shown in Fig. 4(b), with the increase in glucose content, the ratio of the diffraction peak intensities of the 104 and 110 crystal planes of Fe_2O_3 gradually decreases, that is, Fe-0($I_{(104)}/I_{(110)} = 1.54$) > Fe-0.09($I_{(104)}/I_{(110)} = 1.10$) > Fe-0.27 ($I_{(104)}/I_{(110)}$ = 1.09) > Fe-0.45($I_{(104)}/I_{(110)}$ = 1.06) > Fe-1.35($I_{(104)}/I_{(110)} = 1.03$) > Fe-0.9($I_{(104)}/I_{(110)} = 1.01$) > Fe-1.8($I_{(104)}/I_{(110)} = 0.99$). According to the results of Jin et al. [21], thickness of the template affects the intensity of the XRD peaks and Seo et al. [22] added semiconductor single-walled carbon nanotubes to perovskite films to control crystal growth. Therefore, this phenomenon can be attributed to the fact that, with the increase in glucose content, the thickness of the carbon template increases, and the crystal growth direction of Fe_2O_3 becomes more favorable for the (110) plane, resulting in a greater increase in the exposed area of the (110) plane compared to that of the (104) plane. The left or right shift of XRD peak positions is mainly related to the change of lattice parameters, and the change of lattice parameters can be caused by a variety of factors, including lattice distortion, stress, phase transition, and nanoscale effect [21]. From the magnified view of the (104) plane in Fig. 4(c), it can be observed that in Fe-0(without added glucose), (104) plane is located at 33.00°. With the addition of glucose (Fe-0.09), this peak shifts right to 33.20°, which may be due to local stress accumulation during hydrothermal reaction causing lattice contraction [23]. As the glucose concentration increased from Fe-0.09 to Fe-1.8 (except for Fe-1.35), the (104) plane gradually shifted from 33.20° to 33.07°, indicating an increase in the proportion of surface atoms of the microspheres and the surface tension led to lattice expansion, which is consistent with the SEM images in Fig. 8. However, the Fe_2O_3 (104) plane of Fe-1.35 is at 2θ values of 33.13°, which shifted slightly to the right compared with Fe-0.9(33.09°) and Fe-1.8 (33.07).

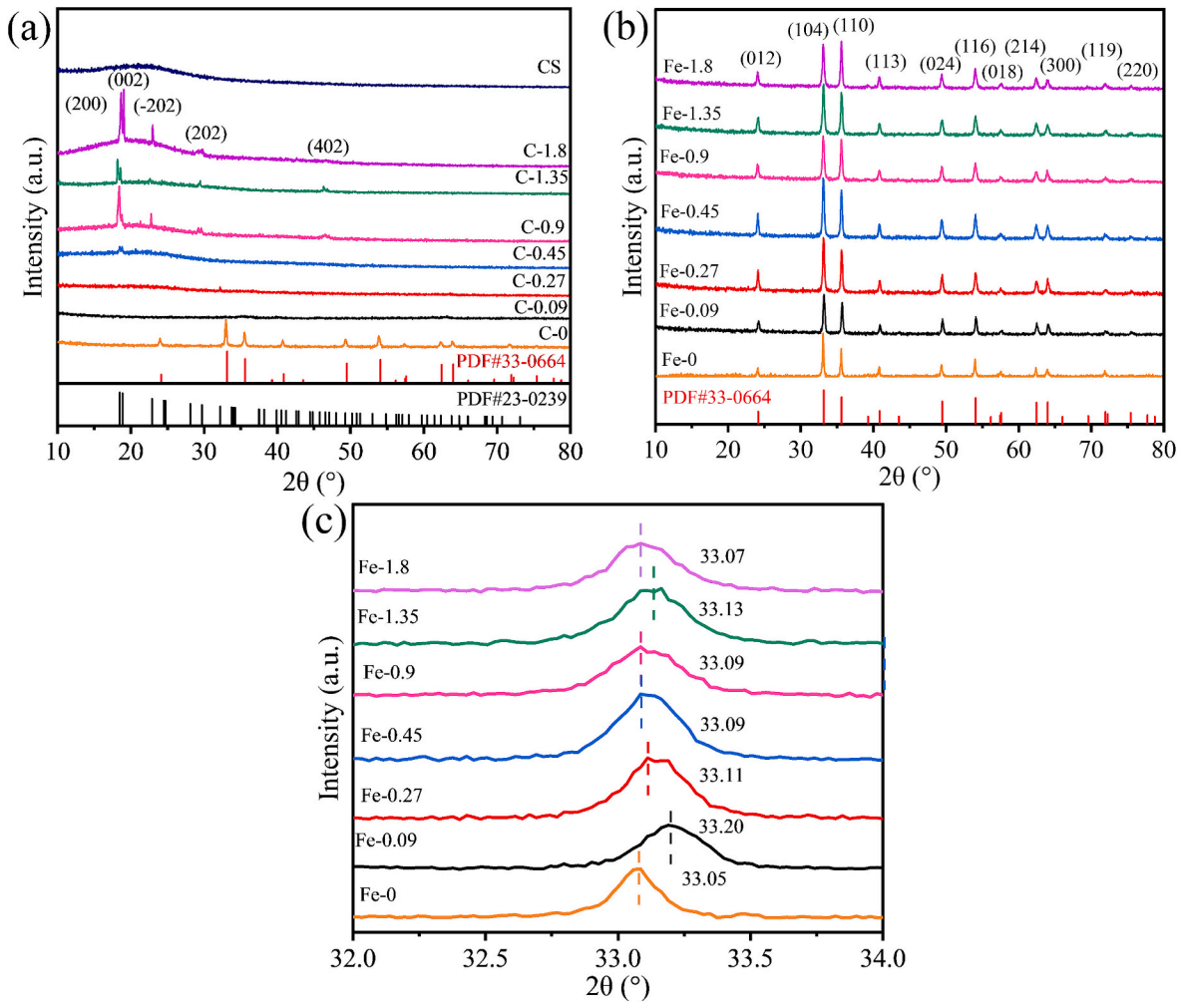

Fig. 4. XRD patterns of samples (a) before, (b) after calcination and amplification pattern (c) in the range of 32–34°.

$$C_6H_{12}O_6 + 6HNO_3 \rightarrow 3H_2C_2O_4 + 6H_2O + 6NO \quad (3)$$

The possible reason for this is that excessive glucose leads to a decrease in carbonization ability, which can only guide the formation of flaky structure Fe_2O_3.

3.2. TG-DTA

Fig. 5 presents the thermal loss mass (TG) and differential thermal analysis (DTA) curves of precursor and Fe_2O_3. As shown in Fig. 3(a), the first stage of weight loss (2.2 %) from 40 °C to 200 °C is mainly the stage of free water released [24,25]. The second stage of weight loss between 200 °C and 450 °C is mainly the thermal oxidation decomposition of organic compounds. During the hydrothermal synthesis process, as the glucose content increases, the weight loss rate of the precursor gradually increases from 10 % of C-0 to 20.1 % (C-0.09), 83.0 % (C-0.27), 85.4 % (C-0.45), 85.6 % (C-0.9), 88.2 % (C-1.35) and 92.1 % (C-1.8). In the DTA curves of the precursor (Fig. 5(b)), the broad endothermic peaks are ascribed to the removal of adsorbed and structural water molecules in the range of 40 °C ~ 200 °C [26]. The primary weight loss between 200 °C and 450 °C, coinciding with the significant exothermic peak, is attributed to the removal of carbon sphere templates. It can be seen from Fig. 5(b), that with the increase of glucose concentration, the DTA curve gradually moves towards the high-temperature zone, and the exothermic decomposition of CS is at 300 °C and 500 °C respectively. Liu et al. [27] suggested that the exothermic peak at low temperature may be attributed to the thermal decomposition of glucose oligomers, while the exothermic peak at high temperature belongs to the thermal decomposition of carbon nuclei. On this basis, it can be known that during the hydrothermal reaction process, as the concentration of glucose in the solution increases, it is more conducive to the formation of glucose polymers. Moreover, among the products of the hydrothermal reaction of glucose, there are both glucose polymers and the formation of carbon nuclei.

Fig. 5(c) and (d) show the TG and DTA traces of the as-synthesized Fe_2O_3. In Fig. 5(c), the first stage of weight loss in the temperature ranges from 40 °C to 200 °C, was attributed to the evaporation of free water. The second stage of weight loss in the temperature range from 200 °C to 470 °C, may be due to the dehydration of lattice hydroxyl groups strongly bound to hematite nanoparticles [28,29]. However, interestingly, in the third stage of the TG curve from 600 °C to 800 °C, there is still a weight loss of 0.2 % to 0.5 %, and there is an exothermic peak on the DTA curve. There may be three reasons for this phenomenon: 1. The oxidation and decomposition of CS wrapped inside Fe_2O_3 cannot be ruled out. This process involves both weight loss and exothermic. However, it can also be seen from Fig. 5(a) that the generation of Fe_2O_3 will restrict the growth of CS particle size, causing the thermal decomposition temperature to shift towards lower temperatures, and the weight loss mainly occurs between 200 and 450 °C. Hossain et al. [10] also pointed out that fructose would completely

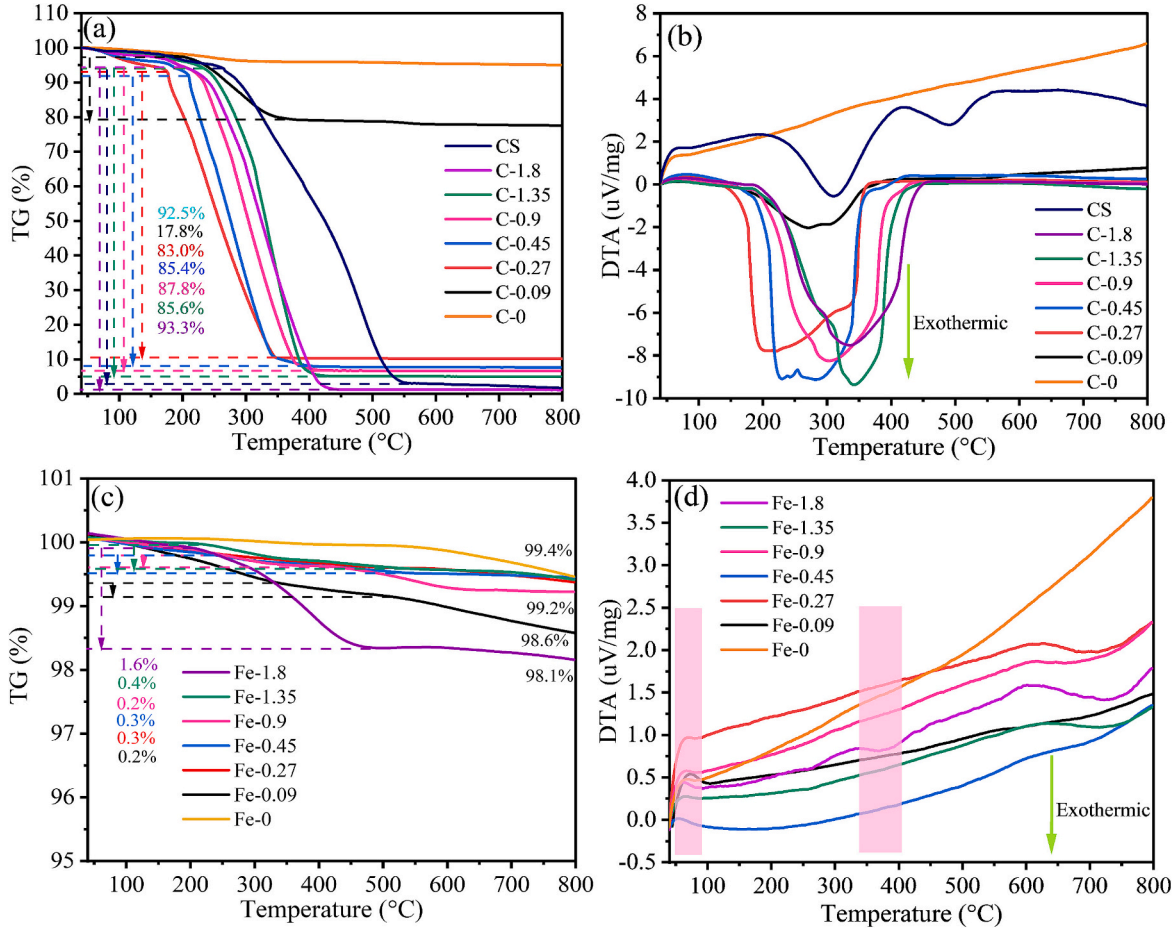

Fig. 5. TG and DTA curves of samples (a and b) before and (c and d) after calcination.

decompose at temperatures below 500 °C by hydrothermal synthesis of hollow Fe_2O_3 from fructose. 2. Crystal form transformation, a process accompanied by weight loss and exothermic simultaneously. Angadi et al. [30] prepared α-Fe_2O_3 by calcining a mixture of glucose and ferric nitrate at 460 °C. They found that although there was only a diffraction peak of α-Fe_2O_3 in the XRD pattern (JCPDS No. 33–0664). However, the Mössbauer spectroscopy indicates that Fe_2O_3 is composed of approximately 50 % α-Fe_2O_3 and 50 % γ-Fe_2O_3. Among them, the smaller exothermic peak can be attributed to the transformation from γ-Fe_2O_3 to α-Fe_2O_3 [31]. A small amount of weight loss can be attributed to the decomposition of hydroxyl groups beneath Fe atoms on the surface of γ-Fe_2O_3 crystals, as confirmed and reported by Tian et al. [32]. 3. Crystal growth, which only accompanied by exothermic. The framework of γ-Fe_2O_3 is similar to that of Fe_3O_4 and has cation vacancies. The Fe^{3+}

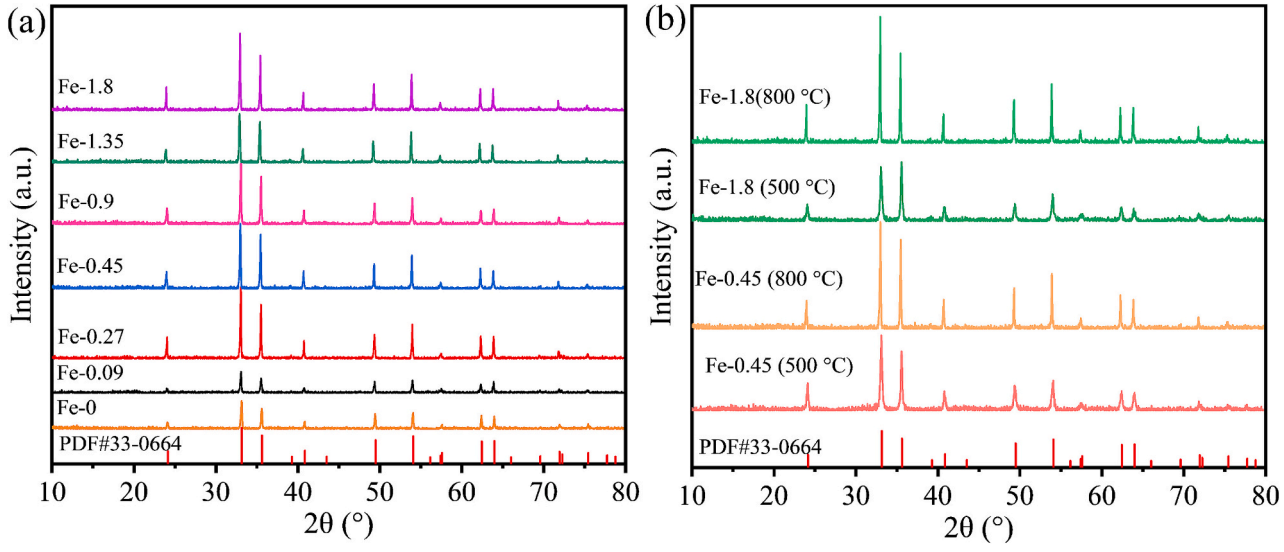

Fig. 6. XRD patterns of (a) Fe_2O_3 calcined at 800 °C and (b) comparison of Fe-0.45 and Fe-1.8 at 500 and 800 °C.

cations occupy all of the tetrahedral (8a) and partial of the octahedral (16d) sites, and the other octahedral (16d) sites are vacant [32,33]. Upon heating, this structure undergoes a transformation to hematite, which has a more ordered rhombohedral lattice structure. Furthermore, Sara et al. [34] pointed out that the increase in calcination temperature supports diffusion of atoms at the grain boundaries and the growth of crystals, which is manifested as a strong shrinkage of the half-peak width and an increase in the average crystallite size. Furthermore, the priority orientation of the crystal planes will change from the index peak of (104) to that of (110), which is consistent with Fig. 6.

3.3. FTIR

Glucose, which can be react under hydrothermal conditions, is used as a shape-directing agent [35]. In addition, as demonstrated above, glucose plays a crucial role in the formation of hollow Fe_2O_3, and it is verified whether the weight loss and exothermic of Fe-X above 600 °C is caused by glucose oligomers or carbon nuclei. Therefore, the surface functional groups of samples before and after calcination were investigated by FTIR, as shown in Fig. 7.

In Fig. 7(a), the infrared spectrum of CS displays a broad peak at 3300 cm^{-1}, which is attributed to -OH stretching vibration [36]. The transmission peaks were observed at 2923 and 2853 cm^{-1}, corresponding to the stretching vibration modes of the $-CH_2$ group [37]. The bands at 1697 cm^{-1} can be attributed to C═O (carbonyl, quinone, ester, or carboxyl) groups [38,39]. The bands positioned at 1607, 1514 and 1455 cm^{-1} are attributed to C═C vibrations [40,41]. The bands at 1297, 1190 and 1089 cm^{-1} correspond to C—O (ester or ether) stretching, while the band at 1023 cm^{-1} is characteristic furan band (1030 to 1015 cm^{-1}) [39,41]. The peak at 973 cm^{-1} is assigned to out-of-plane bending vibrations of C—H in RCH=CHR groups [42]. The band at 800 cm^{-1} is assigned to aromatic C—H out-of-plane bending vibrations [39]. The data is shown in Table 1. A comparison between CS and glucose reveals that glucose underwent dehydration and aromatization during the carbonization process. As reported by Sevilla et al. [36], the intensity of the spectral bands corresponding to the hydroxyl or carboxyl groups in the carbonyl (at 3000–3700 cm^{-1} and 1000–1450 cm^{-1}) is weaker than that of the corresponding sugar bands, thus revealing the dehydration reaction. New vibration bands at 1697 cm^{-1}, corresponding to C═O groups, and at 1607, 1514 and 1455 cm^{-1}, corresponding to C═C groups, appear in the CS. The appearance of the bands at 1620 and 1513 cm^{-1} reveals the aromatization of the samples. The results demonstrated the presence of numerous -OH, C═O and C_6H_5-C=O groups on the surface of the glucose hydrochar. Thus, the electrostatic interactions or coordination between the carbonaceous spheres and the adsorbed metallic ions lead to the formation of the core-shell composite [10,43,44].

Table 1
Distribution of infrared frequencies and functional groups in the range of 4000 to 500 cm^{-1}.

Sample	FTIR peaks (cm^{-1})	Peak assignments
CS	3300	υ(O—H)
	2923, 2853	υ_{as} ($-CH_2$), υ_s ($-CH_2$)
	1697	υ(C=O)
	1607, 1514, 1455	υ(C=C)
	1297, 1190, 1089	υ(C—O)
	973, 800	δ(C—H)

The surface functional groups of the samples after calcination were analyzed by Fourier Transform Infrared Spectroscopy (FTIR) under different glucose concentrations, as shown in Fig. 7(b). A peak at around 600 cm^{-1} was observed, which is assigned to the stretching vibrational mode of the Fe—O bond [45]. As the concentration of anhydrous glucose increases, there is a gradual leftward shift in the Fe—O peak position, specifically: 591 cm^{-1} (Fe-0.09) → 615 cm^{-1} (Fe-0.27) → 616 cm^{-1} (Fe-0.45) → 625 cm^{-1} (Fe-0.9) → 627 cm^{-1} (Fe-1.35) → 638 cm^{-1} (Fe-18). As glucose concentration increases from 0.09 M to 1.8 M, the microstructure of the sample undergoes a gradient evolution from discrete particles to uniform hollow spheres; during calcination, this dense and ordered hollow structure may shift the Fe—O bond from 591 cm^{-1} to 638 cm^{-1} by optimizing lattice reorganization kinetics, enhancing local symmetry, and alleviating internal stress. Furthermore, in the samples after the calcination process, no organic functional groups of glucose and its derivatives were observed. It is indicated that no organic functional groups or the concentration of organic functional groups is lower than the detection limit of FTIR on the surface of the samples after the calcination process.

3.4. SEM

To further clarify the influence of glucose concentration on the morphology of the precursors, the SEM images and particle size distribution results of carbon precursor samples at different concentrations are shown in Figs. 8(a-f) and 9(a-f), respectively. As shown in Fig. 8(a), under the condition of lower glucose concentration (C-0.09), the samples are mainly composed of irregular carbon fragments and agglomerated particles, with a relatively small average particle size (D_{50} = 61.62 nm) and distribution ranges from 30 nm to 110 nm, indicating

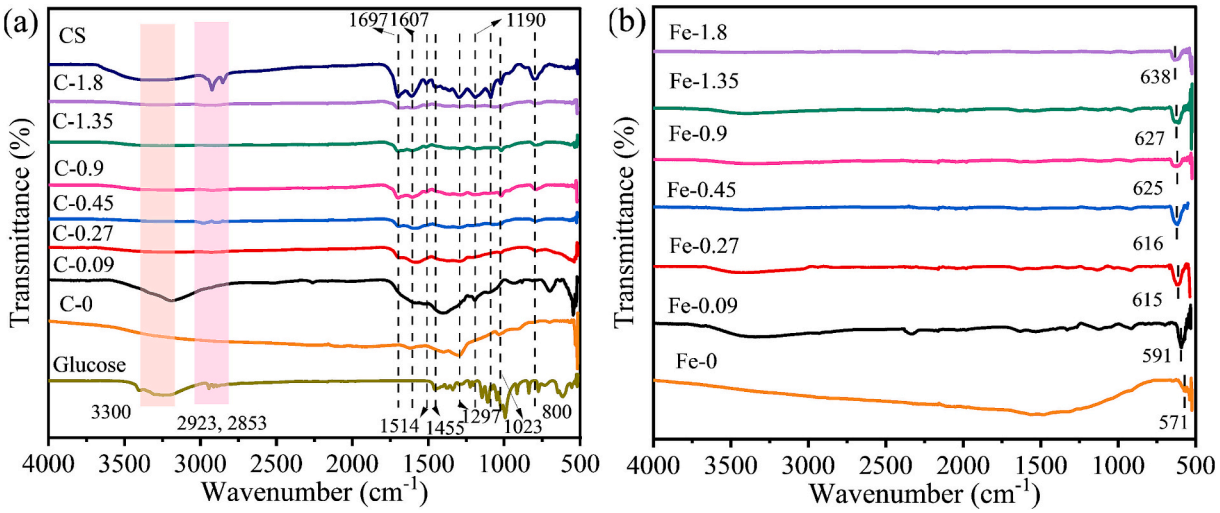

Fig. 7. FTIR spectra of samples (a) before and (b) after calcination.

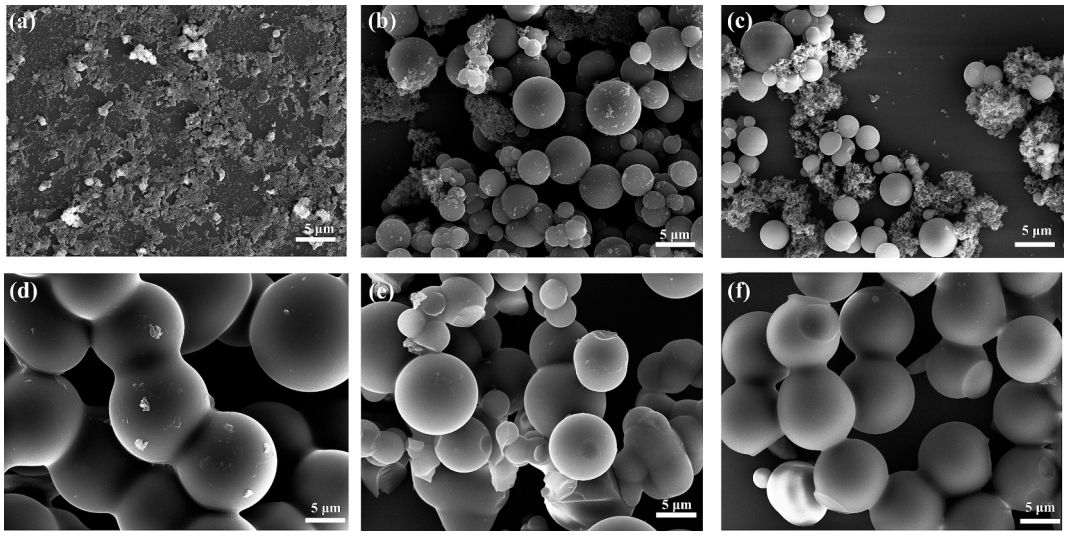

Fig. 8. SEM images of (a) C-0.09, (b) C-0.27, (c) C-0.45, (d) C-0.9, (e) C-1.35 and (f) C-1.8.

incomplete dehydration and condensation of glucose and carbonization reactions. With the increase of glucose concentration (C-0.27 and C-0.45), the carbon spheres become more uniform in morphology and smooth on the surface, with a significant increase in average particle size (D_{50} = 3.73 μm and 2.82 μm), and distribution ranges from 1 μm to 7 μm (Figs. 9b–c), suggesting a denser and more ordered carbon sphere structure. These regular carbon spheres can serve as ideal soft templates, providing conditions for the uniform adsorption of Fe^{3+} and the formation of hollow structures. When the glucose concentration is further increased (C-0.9 to C-1.8), excessive carbonization and rapid gas release during calcination lead to partial fusion or deformation of the carbon spheres (Figs. 8d–f), with a slight decrease in average particle size (D_{50} = 10.55 μm → 7.81 μm) and distribution ranges from 5 μm to 12 μm.

The morphology evolution and particle size distribution of hollow Fe_2O_3 under varying glucose concentrations were systematically investigated through SEM analysis. As demonstrated in Fig. 10, six distinct samples (Fe-0.09, Fe-0.27, Fe-0.45, Fe-0.9, Fe-1.35 and Fe-1.8) exhibited morphology transformations directly correlated with glucose concentration. Fig. 10(a) is the SEM image of the sample at a glucose concentration of 0.09 M. It is evident that the Fe-0.09 is composed of many highly dispersed Fe_2O_3 nanoparticles with a rough surface. When the glucose concentration is increased to 0.27 M, the prepared Fe_2O_3 sample is agglomerated, forming a "mushroom"-shaped aggregate with a rough surface, as shown in Fig. 10(b). Further increasing the glucose concentration to 0.45 M, as shown in Fig. 10(c), the region observed by SEM in the Fe-0.45 showed a spherical shape, relatively uniform structure, smooth surface and a pore of about 400 nm. However, as the concentration of glucose in the solution continues to increase, the hollow Fe_2O_3 microspheres begin to break significantly, with the surface becoming rougher and the proportion of broken hollow Fe_2O_3 microspheres gradually increasing, as shown in Fig. 10(d) and (e). It is worth noting that the hollow structure inside the broken Fe_2O_3 microspheres

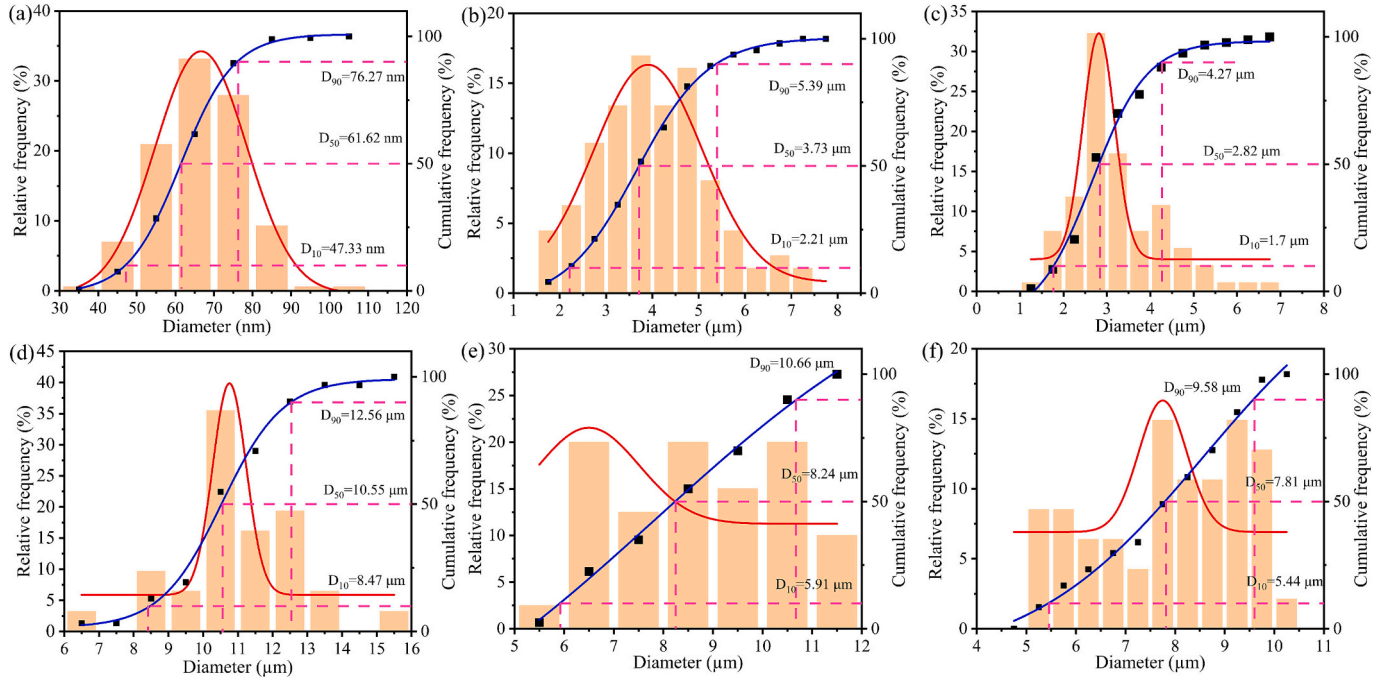

Fig. 9. Particle size distributions of (a) C-0.09, (b) C-0.27, (c) C-0.45, (d) C-0.91, (e) C-1.35 and (f) C-1.8.

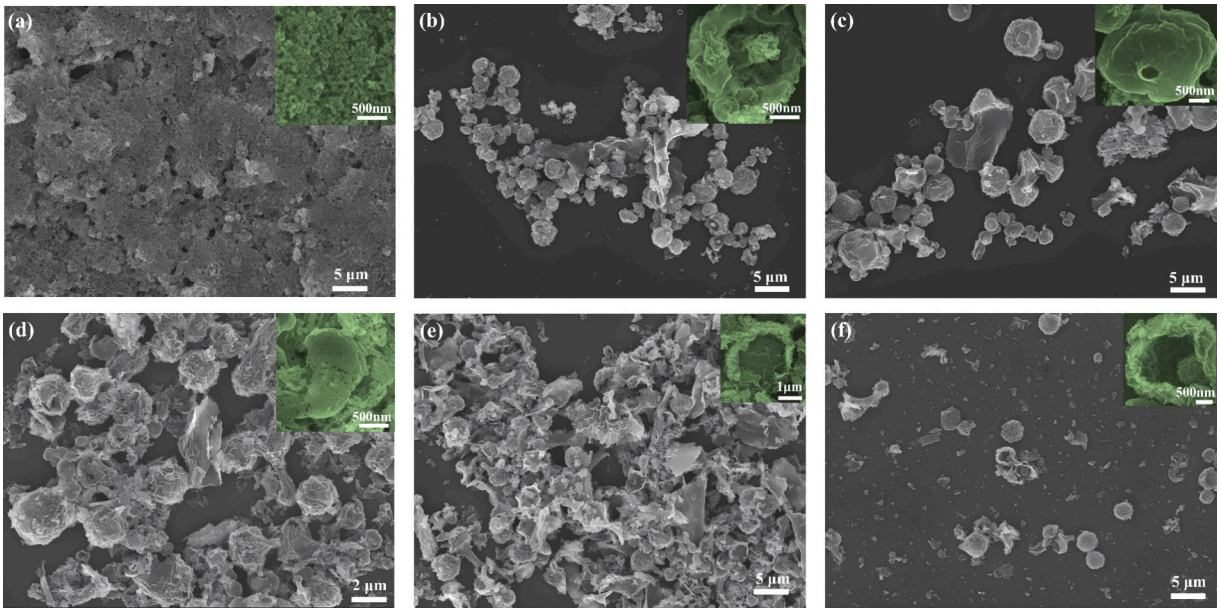

Fig. 10. SEM images of (a) Fe-0.09, (b) Fe-0.27, (c) Fe-0.45, (d) Fe-0.91, (e) Fe-1.35 and (f) Fe-1.8.

can still be clearly observed in the SEM images. When the concentration of glucose in the solution reaches 1.8 M, as shown in Fig. 10(f), it is difficult to observe broken hollow Fe_2O_3 microspheres in the entire field of view.

As shown in Fig. 11, the particle size distribution of the prepared samples, as well as the average particle size and average crystallite size, are presented in Table 2. In Fig. 11(a), the particle size distribution of the Fe-0.09 sample is concentrated at the nanoscale, with D_{10}, D_{50}, and D_{90} values of 48.02 nm, 66.78 nm, and 88.36 nm, respectively, indicating a narrow and uniform particle size distribution, possibly due to insufficient glucose, lacking a template effect, which makes it difficult for microspheres to grow, resulting in only dense small nano-particles. As the glucose concentration increases to 0.27 M, the microsphere size significantly increases and transitions to micrometer scale, with D_{50} in Fe-0.27 increasing to 1.71 μm, showing evident particle growth. At this point, the glucose structural guiding ability enhances, promoting particle agglomeration and forming micrometer-sized hollow spheres. In Fig. 11(c), particle size further increases (D_{50} = 2.49 μm), the hollow structure gradually becomes more apparent. But the particle size distribution becomes wider. In Fig. 11(d), the average particle size of Fe-0.9 slightly decreases (D_{50} = 1.18 μm), suggesting that high glucose concentration (0.9 M) may lead to excessive precursor deposition, inhibiting uniform spherical structure growth, thus causing strong aggregation and structural collapse of microspheres (Fig. 10(d)). When the glucose concentration further increases to 1.35 M and 1.8 M (Figs. 10(e)–(f)), the microsphere size slightly decreases, with D_{50} of Fe-1.35 being 2.05 μm and D_{50} of Fe-1.8 being 1.14 μm, indicating that under high glucose concentration conditions, excessive carbon coating or excessive gas

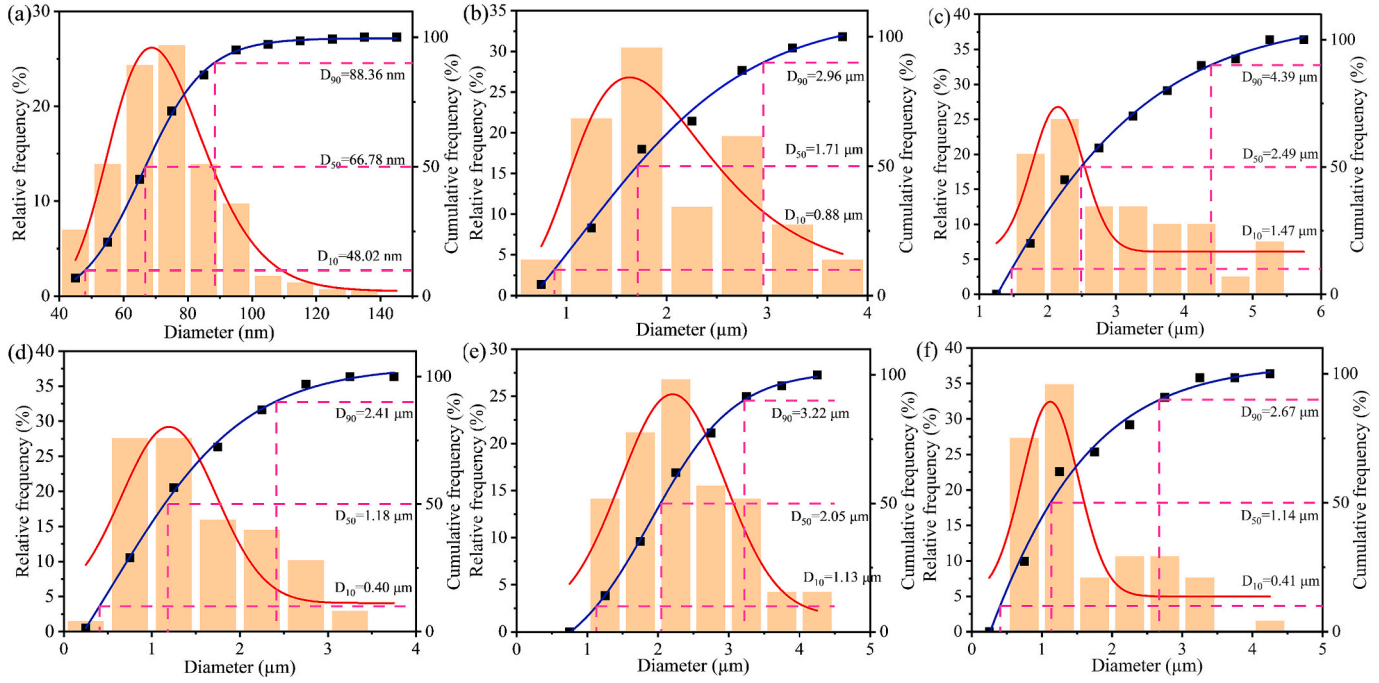

Fig. 11. Particle size distributions of (a) Fe-0.09, (b) Fe-0.27, (c) Fe-0.45, (d) Fe-0.91, (e) Fe-1.35 and (f) Fe-1.8.

Table 2
Average particle size and average crystallite size.

Sample	Fe-0.09	Fe-0.27	Fe-0.45	Fe-0.9	Fe-1.35	Fe-1.8
Average particle size [a]	72.83 nm	2.10 μm	2.99 μm	1.60 μm	2.38 μm	1.57 μm
Average crystallite size [b]	40.9 nm	41.3 nm	41.4 nm	35.6 nm	36.4 nm	38.6 nm
lattice strain [c]	−0.00027	0.0013	0.00071	0.00059	0.00068	0.00039
Average crystallite size [c]	31.64 nm	51.33 nm	38.39 nm	32.92 nm	32.31 nm	32.38 nm

[a] : Statistics on particle size from the SEM image.
[b] : The crystallite size was calculated using the Scherrer formula based on the XRD data.
[c] : The crystallite size was calculated using the W—H based on the XRD data.

generation leads to the collapse of hollow structures, thereby inhibiting further particle growth. Additionally, Figs. 11(e)–(f) show that the particle morphology tends to become irregular, which may also be a reason for the decrease in particle size and increased polydispersity.

According to the crystallite size calculated from XRD (Table 2), the crystallite sizes of all samples range from 35.6 to 41.4 nm, indicating that the calcination conditions are well controlled, with no obvious sintering agglomeration phenomena. Notably, the Fe-0.45 sample, while achieving the maximum average particle size (2.99 μm), also has a large crystallite size (41.4 nm), further verifying that 0.45 M glucose is conducive to the synergistic optimization of hollow microsphere formation and crystal growth.

Fig. 12 shows the relationship curve of βcosθ and 4sinθ measured by the W—H method for Fe-0.27, Fe-0.45, Fe-0.91, Fe-1.35 and Fe-1.8. This curve is used to measure the crystal diameter and lattice strain of nanomaterials. The results show (see Table 2) that the slope of the Fe-0.09 sample is slightly negative ($\varepsilon = -2.7 \times 10^{-4}$), indicating that it is mainly dominated by the size effect. As the glucose concentration increases to 0.27 M, the average crystallite size significantly increases (51.33 nm), and the micro-strain rises to 1.3×10^{-3}, suggesting that the crystallite growth is completer and more accompanied by a slight tensile strain, which may be related to the formation of the carbon template. For the Fe-0.45 sample, both D and ε are in a moderate range (38.39 nm, 7.1×10^{-4}), and the sample presents a relatively regular hollow structure, indicating a good balance between crystallite growth and strain, and the carbon template assists in forming uniform hollow spheres. When the glucose concentration is further increased, the average crystallite sizes of Fe-0.9 and Fe-1.35 decrease to 32.92 nm and 32.31 nm respectively, while the micro-strains decrease to 5.9×10^{-4} and 6.8×10^{-4} respectively. The SEM images show that the sample morphology is irregular, with cracks, agglomeration and voids, indicating that excessive glucose leads to the instability of the carbon template, which limits the crystallite growth and aggravates the lattice distortion and structural defects. In Fe-1.8, the average crystallite size is 32.38 nm and the micro-strain is 3.9×10^{-4}, although it has slightly decreased, the sample still has surface defects and local fractures, and the structure is not uniform. The slight decrease in strain may be related to the structural collapse or stress relaxation caused by defect formation.

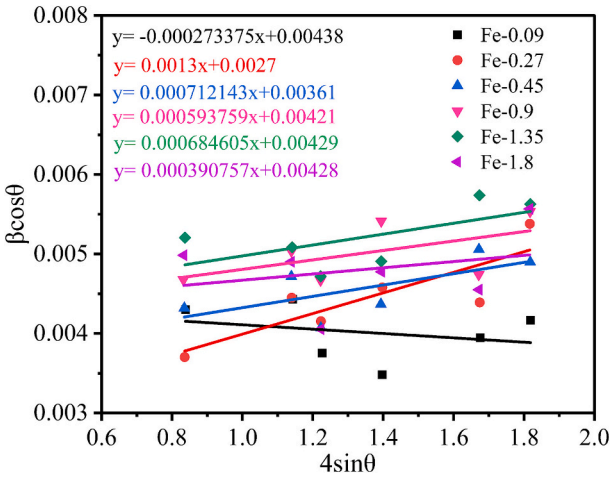

Fig. 12. Plotting of βcosθ vs 4sinθ of W—H analysis, for Fe-0.09, Fe-0.27, Fe-0.45, Fe-0.91, Fe-1.35 and Fe-1.8.

These are due to the increase in glucose concentration, leading to larger carbon spheres. Metal ions adsorb around these carbon spheres. If the carbon spheres are too small, they cannot form spherical structures and if they are too large, metal ions cannot fully encapsulate them. During high-temperature calcination, the carbon spheres disappear and the metal oxides fail to support the formation of spherical structures. Li et al. [46] reported that the size of CS increases with the rise in glucose concentration. According to the LaMer model and Ostwald ripening mechanism [47,48], at low concentrations, there are fewer glucose molecules, resulting in the formation of numerous small crystal nuclei. However, due to the limited glucose concentration, each nucleus cannot grow sufficiently, ultimately forming smaller carbon spheres. With an abundant carbon source, continuous growth is supported, leading to an increase in the diameter of the carbon spheres. Luo et al. [39] investigated four distinct growth stages of PCNs, starting with the formation of nanonuclei, which then aggregate to form larger nuclei (primary cores). These primary cores grow further by colliding and merging with other cores, ultimately resulting in particle formation.

3.5. Bet

Additionally, the morphological changes will inevitably influence the specific surface area of the prepared samples. In order to explore the surface area and pore size distribution, nitrogen adsorption-desorption isotherm tests were conducted on the hollow Fe_2O_3 obtained under different glucose concentrations and the results are shown in Fig. 13. In Fig. 13(a), the isotherm was classified as type III according to IUPAC, indicating the successful synthesis of microspheres characterized by a loose and inhomogeneous structure [12,49]. These pores could be formed by the aggregation of nanocrystals in the walls of hollow structures, while others might derive from natural voids existing in single-crystalline Fe_2O_3. Moreover, the concave curve indicated strong interactions between adsorbed molecules. The adsorbent-adsorbate interactions were relatively weak and the adsorbed molecules were clustered around the most favorable sites on the surface of a nonporous or macroporous solid [49]. Furthermore, the hysteresis loop of the materials coincided with the type H3, further supporting their mesoporous nature [50]. The BET surface area and average pore size of the samples are shown in Table 3. The specific surface area of Fe-0.09 is 19.7 m^2/g, with an average pore size of 37.9 nm, indicating a predominance of macropores. As the glucose concentration increases to 0.27 M (Fe-0.27), the specific surface area significantly rises to 25.2 m^2/g, while the average pore size decreases to 25.3 nm, suggesting a more uniform pore structure transitioning towards mesopores. For Fe-0.45 and Fe-0.9, there is little change in specific surface area (20.1 and 19.8 m^2/g), with the average pore size further decreasing to 20.3 nm and 19.7 nm, respectively, indicating a further contraction of the pore structure, trending towards a more uniform mesopore range. The specific surface area of Fe-1.35 drops to its lowest value (16.5 m^2/g), while the average pore size increases back to 25.04 nm, possibly due to partial rupture or collapse of

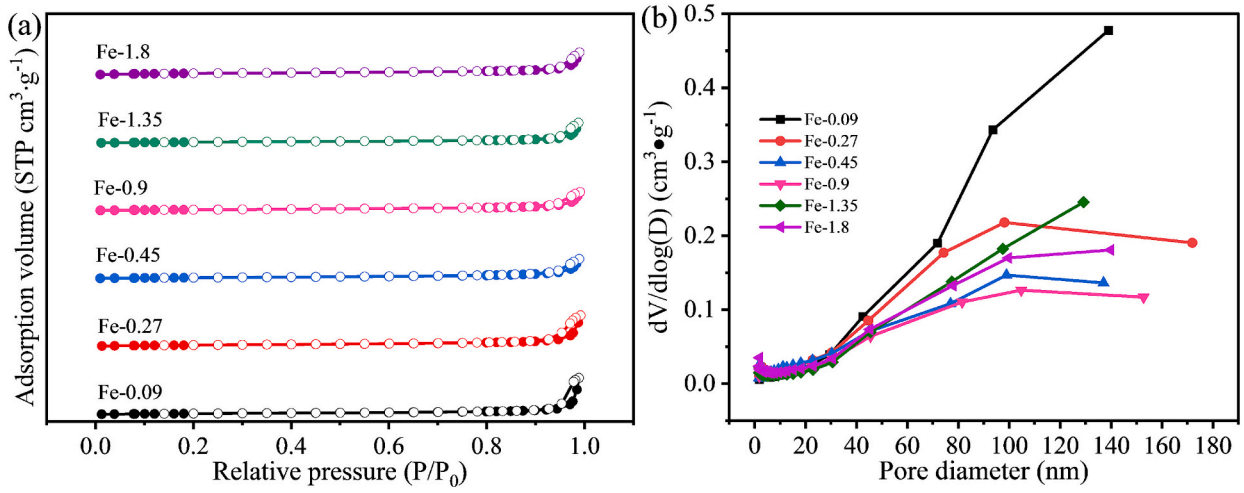

Fig. 13. (a) Nitrogen adsorption-desorption isotherm and (b) Pore distribution.

Table 3
The specific surface area, pore volume and average pore diameter of the samples prepared.

Sample	Surface areas (m^2/g)	Average pore diameter (nm)
Fe-0.09	19.7	37.9
Fe-0.27	25.2	25.3
Fe-0.45	20.1	20.3
Fe-0.9	19.8	19.7
Fe-1.35	16.5	25.1
Fe-1.8	24.9	18.5

spherical structures, leading to a relative increase in macropore numbers. For Fe-1.8, the specific surface area again increases to 24.9 m^2/g, with pore size reducing to 18.5 nm. Excessive organic aggregation or gas disturbance may cause structural damage, resulting in pore structure instability.

3.6. XPS

XPS analysis was performed to evaluate the surface chemical composition of the hollow Fe_2O_3 microspheres. Fig. 14(a) presents the wide spectrum, showing the signals of Fe, O and C. Atomic ratio of lattice oxygen(O_L), oxygen vacancies(O_V), chemisorbed oxygen(O_C), Fe^{2+} and Fe^{3+} calculated from XPS results in Table 4, while based on the fact that there are no characteristic peaks for organic functional groups in the FTIR characterization, it is speculated that carbon-containing bonds may originate form the carbon tape used during the XPS sample preparation. From Fig. 14(b), the peaks observed around at 727 eV and 713 eV are characteristic features of Fe^{3+}, originating from the 2p 1/2 and 2p 3/2 orbitals, respectively [51,52]. Furthermore, the deconvolution peak observed around at 709 eV and 722 eV correspond to Fe^{2+}, which may be attributed to the formation of O_V in Fe_2O_3 [53,54]. The creation of O_V in the crystalline lattice results in two electrons remaining on the missing oxygen atom, which facilitates the reduction of Fe^{3+} to Fe^{2+} [53,55]. Besides, it is evident that the main peak of Fe 2p3/2 in the Fe-0.09 sample is located at 712.48 eV, while in the Fe-0.45 and Fe-0.9 samples, this peak shifts to 713.68 eV and 714.03 eV respectively, indicating a significant change in the chemical environment of Fe^{3+}. Combining the data on O_V content from Table 4 (Fe-0.09 at 26.52 %, Fe-0.45 and Fe-0.9 at 21.69 % and 18.15 % respectively), it can be inferred that the reduction in O_V leads to a decrease in electron cloud density around iron atoms, weakening the shielding effect, which consequently increases the binding energy of Fe 2p [56,57]. The main peak of Fe 2p3/2 in the Fe-1.8 sample slightly decreases to 713.28 eV, although its O_V content significantly increases to 65.07 %, possibly due to the higher oxygen vacancy-induced electronic structure rearrangement, which to some extent regulates the local charge distribution.

Fig. 14(c) shows that the high-resolution spectrum of O 1 s mainly includes three peaks, corresponding to O_L, O_V and O_C [57]. The O_L peak of the Fe-0.09 sample appears at 527.85 eV, shifting to 529.32 eV in Fe-0.45 and 530.04 eV in Fe-0.9 as glucose concentration increases, indicating a significant rise in binding energy. In the Fe-1.8 sample, the peak slightly rises to 530.38 eV. According to Table 4, the lattice oxygen ratio of Fe-0.09 is 12.44 %, with a high O_V content (26.52 %), leading to an enhanced electron cloud density and consequently lower binding energy for O 1 s [58]. With the reduction of O_V (Fe-0.45 and Fe-0.9 at 21.69 % and 18.15 % respectively), oxygen atoms are in a more complete coordination environment, leading to an increase in the O 1 s binding energy. In the Fe-1.8 sample, the proportion of O_V significantly increased to 65.07 % and the proportion of O_L also rose to 23.69 %, resulting in a slight increase in the binding energy of the O 1 s peak. O_C is formed due to the adsorption of water and hydroxyl groups of FeOOH on the surfaces of α-Fe_2O_3 and γ-Fe_2O_3. The presence of O_C in XPS proves the existence of FeOOH in Fe_2O_3, indicating that in Fig. 5(c), the slight weight loss above 600 °C might be caused by the high-temperature decomposition of FeOOH in the particle phase of Fe_2O_3. Furthermore, it is worth noting that the content of O_V is positively correlated with the exothermic intensity shown in Fig. 5(d) above 600 °C. This also proves that the exothermic reaction of Fe_2O_3 above 600 °C might be caused by the lattice transformation from γ-Fe_2O_3 to α-Fe_2O_3.

3.7. Reaction mechanism

Based on FTIR, XRD and SEM observation, the possible forming mechanism of hollow Fe_2O_3 microspheres is schematically illustrated in Fig. 15. During the hydrothermal process, glucose undergoes dehydration, condensation and carbonization reactions to form carbonaceous intermediates, which can act as soft templates to adsorb Fe^{3+}. Meanwhile, partial redox reactions occur between Fe^{3+}, NO_3^- and the glucose intermediates, generating small organic acids and reducing some Fe^{3+} to Fe^{2+}. The combined results of W—H and SEM show that the crystallite size of Fe_2O_3, lattice strain and the morphology of the carbon precursor are significantly affected by the glucose concentration. At 0.09 M, the carbonization reaction is incomplete, and the irregular carbon fragments generated can only partially adsorb Fe species [43], leading to uneven nucleation, restricted crystallite growth and the generation of compressive strain. After calcination, dispersed Fe_2O_3 nanoparticles are formed. As the glucose concentration increases, the generated carbon spheres have a uniform and continuous structure, and are rich in

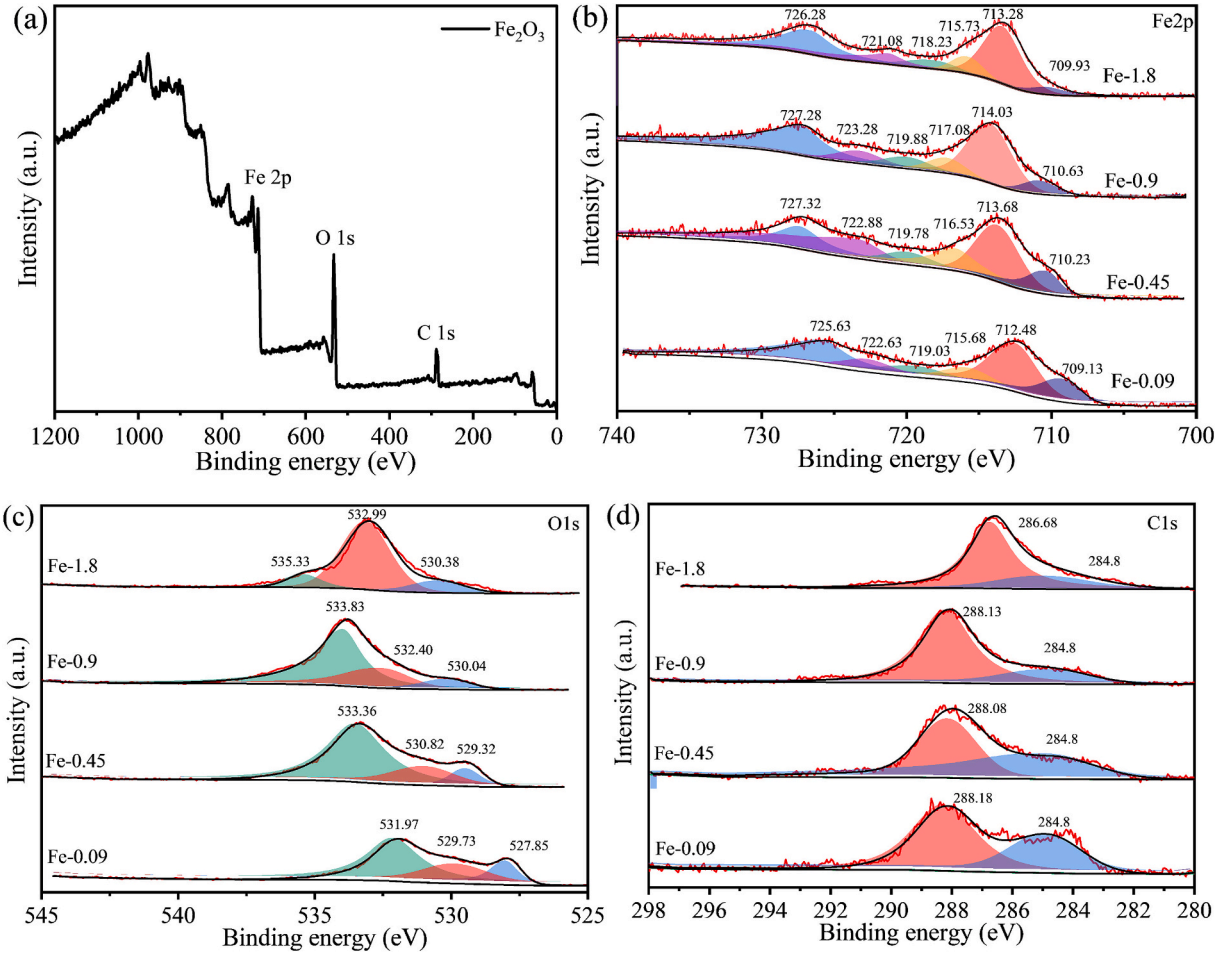

Fig. 14. XPS of (a) Survey spectrum, (b) Fe 2p (c) O 1 s and (d) C 1 s.

Table 4
XPS analyses of the surface concentration for samples.

Samples	Atomic concentration (%)		X_O (%)		
	Fe	O	O_L	O_V	O_C
Fe-0.09	33.06	66.94	12.44	26.52	61.04
Fe-0.45	31.56	68.44	8.10	21.69	70.21
Fe-0.9	31.80	68.20	14.24	18.15	67.25
Fe-1.8	29.85	70.15	23.69	65.07	11.24

hydroxyl, carboxyl and other oxygen-containing functional groups, which can act as flexible templates to buffer lattice distortion, promote the outward diffusion of Fe species and the inward oxidation of carbon, thereby generating hollow Fe_2O_3 microspheres with smaller strain and regular structure. When the glucose concentration is too high (1.35 M and 1.8 M), rapid carbonization and intense gas release cause the carbon spheres to fuse and deform, generating structural stress and hindering the migration of Fe species, resulting in overly thin shells or partially collapsed structures. Therefore, an appropriate glucose concentration (0.45 M) can achieve a balance between redox equilibrium, the stability of the carbon template and the controllability of crystal growth, thereby promoting the ordered formation of hollow Fe_2O_3 microspheres.

Following calcination, this process will generate hollow iron oxide structures, which aligns with the results in references [10, 37–39, 59].

4. Conclusions

In Conclusion, by regulating the glucose concentration in the reaction system, the formation process and final morphology of Fe_2O_3 nanostructures can be precisely controlled: at low concentrations (<0.45 M), basic nanoparticles are formed, at moderate concentrations, a dynamic equilibrium mechanism promotes the uniform wrapping of the core by the carbon layer and self-assembles into regular microsphere structures; while at excessively high concentrations (>0.45 M), the structure becomes unstable due to excessive growth of the carbon layer. During the reaction, the organic acids generated from the oxidation of glucose combine with Fe^{3+} or Fe^{2+} (Reduction from Fe^{3+}) to form a metal-organic intermediate phase, and the thermodynamic evolution of this intermediate phase ultimately results in a single α crystal phase. The final morphology of Fe-0.45 is smooth and rounded, with an average particle size of 2.88 μm, an average pore diameter of 20.3 nm, and a specific surface area of 20.1 m^2/g.

CRediT authorship contribution statement

Hong Yin: Writing – original draft. **Linfei Yu:** Investigation. **Jiahui Zheng:** Formal analysis. **Chenliang Zhou:** Writing – review & editing, Funding acquisition. **Wenxiu He:** Formal analysis. **Gewen Yu:** Funding acquisition, Conceptualization. **Jian Ding:** Funding acquisition, Conceptualization. **Qiang Zhang:** Investigation. **Quansheng Liu:** Validation.

Declaration of competing interest

The authors declare that they have no known competing financial interests or personal relationships that could have appeared to influence

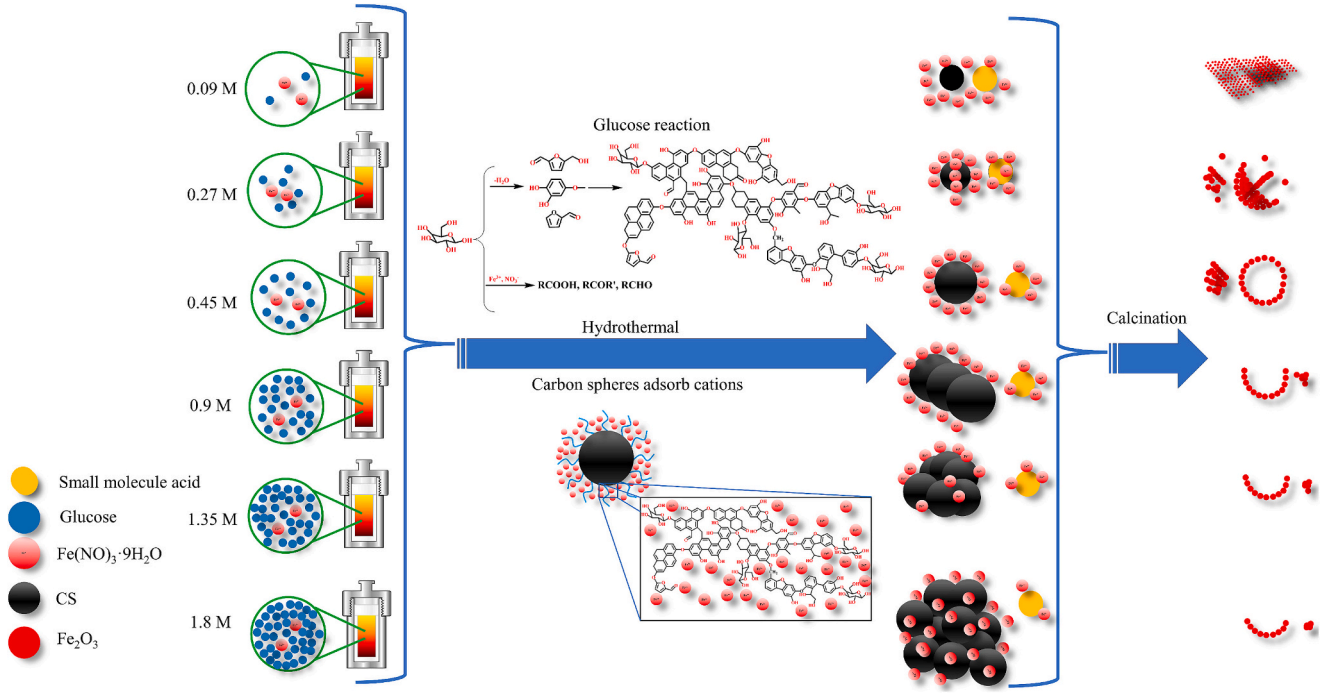

Fig. 15. Schematic illustration of the mechanism of hollow Fe_2O_3 by a hydrothermal process.

the work reported in this paper.

Acknowledgements

This work was financially supported by the Natural Science Foundation of Inner Mongolia Autonomous Region (2024MS02015), Project of Basic Research Operating Costs of Colleges and Universities (2024XKJX002) and the Program for Young Talents of Science and Technology in Universities of Inner Mongolia Autonomous Region (Grant No. NJYT22070). We are grateful to Associate Professor Na Li form the School of Chemical Engineering at IMUT(Inner Mongolia University of Technology) for her support in XPS testing and analysis.

Data availability

Data will be made available on request.

References

[1] J. Wang, L. Zhang, C. Li, Superhydrophobic and mechanically robust polysiloxane composite coatings containing modified silica nanoparticles and PS-grafted halloysite nanotubes, Chin. J. Chem. Eng. 52 (2022) 56–65, https://doi.org/10.1016/j.cjche.2021.12.017.

[2] M. Peng, Q. Wang, M. Sha, B. Jiang, D. Zhang, Durable self-cleaning superhydrophobic composite coatings based on fluorine-modified organic polysilazane and SiO_2 particles prepared by facile spraying technique, Chin. J. Chem. Eng. (2025), https://doi.org/10.1016/j.cjche.2025.03.021.

[3] J. Xie, J. Hu, X. Lin, L. Fang, F. Wu, X. Liao, H. Luo, L. Shi, Robust and anti-corrosive PDMS/SiO_2 superhydrophobic coatings fabricated on magnesium alloys with different-sized SiO_2 nanoparticles, Appl. Surf. Sci. 457 (2018) 870–880, https://doi.org/10.1016/j.apsusc.2018.06.250.

[4] E. Huovinen, J. Hirvi, M. Suvanto, T.A. Pakkanen, Micro–micro hierarchy replacing micro–nano hierarchy: a precisely controlled way to produce wear-resistant superhydrophobic polymer surfaces, Langmuir 28 (2012) 14747–14755, https://doi.org/10.1021/la303358h.

[5] C. Li, H. Lai, Z.J. Cheng, J.J. Yan, L.H. Xiao, L. Jiang, M.Z. An, Coating "nano-armor" for robust superwetting micro/nanostructure, Chem. Eng. J. 385 (2020) 123924, https://doi.org/10.1016/j.cej.2019.123924.

[6] P. Yan, Y. Hou, Y. Wu, M. Liu, H. Zheng, Wet chemical-assisted laser texture armored bionic superhydrophobic surfaces with anti-icing/corrosion property, Surf Interfaces 65 (2025), https://doi.org/10.1016/j.surfin.2025.106458.

[7] Y. Lu, J. Li, W. Shi, S. Fu, J. Qi, X. Li, J. Chen, Laser-induced biomimetic honeycomb structures synergizing with nanocomposites to build durable copper-based superhydrophobic coatings, Appl. Surf. Sci. 706 (2025), https://doi.org/10.1016/j.apsusc.2025.163592.

[8] Y. Liu, S. Hu, X. Zhang, S. Sun, Investigation of photoelectrocatalytic degradation mechanism of methylene blue by α-Fe_2O_3 nanorods array, Chin. J. Chem. Eng. 57 (2023) 162–172, https://doi.org/10.1016/j.cjche.2022.08.021.

[9] H. Song, T. Chen, X. Zhang, X. Jia, One-step template-free synthesis of hollow core–shell α-Fe_2O_3 microspheres with improved lithium storage and gas-sensing properties, CrystEngComm 17 (2015) 1173–1181, https://doi.org/10.1039/c4ce01996b.

[10] M.S. Hossain, T. Furusawa, M. Sato, Hydrothermal synthesis, characterization and thermal stability studies of α-Fe_2O_3 hollow microspheres, Adv. Powder Technol. 33 (2022), https://doi.org/10.1016/j.apt.2022.103797.

[11] L. De Los Santos, A. Bustamante Valladares, L. León Domínguez, J.B. Félix, D. G. Kargin, A.L. Mukhambetov, N.O. Kozlovskiy, J. Flores Moreno, R. Castellanos Santibañez, C.H.W. Barnes Cabrera, Characterization and magnetic properties of hollow α-Fe_2O_3 microspheres obtained by sol gel and spray roasting methods, J. Sci-Adv. Mater. Dev. 4 (2019) 483–491, https://doi.org/10.1016/j.jsamd.2019.07.004.

[12] M. Wang, Y. Wang, Y. Mo, Q. Gao, Y. Li, J. Zhu, Novel hollow α-Fe_2O_3 nanofiberswith robust performance enabled multi-functional applications, Environ. Res. 212 (2022), https://doi.org/10.1016/j.envres.2022.113459.

[13] A. Nandagudi, S.H. Nagarajarao, M.S. Santosh, B.M. Basavaraja, S.J. Malode, R. J. Mascarenhas, N.P. Shetti, Hydrothermal synthesis of transition metal oxides, transition metal oxide/carbonaceous material nanocomposites for supercapacitor applications, Mater Today Sustain 19 (2022), https://doi.org/10.1016/j.mtsust.2022.100214.

[14] X. Zhang, Y. Chen, H. Liu, Y. Wei, W. Wei, Facile synthesis of α-Fe_2O_3 hollow sub-microstructures, morphological control and magnetic properties, CrystEngComm 15 (2013), https://doi.org/10.1039/c3ce40579f.

[15] X. Kang, Z. Wu, F. Liao, T. Zhang, T. Guo, Ag/α-Fe_2O_3 hollow microspheres: preparation and application for hydrogen peroxide detection, J. Solid State Chem. 229 (2015) 266–271, https://doi.org/10.1016/j.jssc.2015.06.031.

[16] C. Jin, C. Ge, G. Xu, G. Peterson, Z. Jian, Y. Wei, K. Zhu, Influence of nanoparticle size on ethanol gas sensing performance of mesoporous α-Fe_2O_3 hollow spheres, Mater. Sci. Eng. B 224 (2017) 158–162, https://doi.org/10.1016/j.mseb.2017.07.015.

[17] G. Ischia, M. Cutillo, G. Guella, N. Bazzanella, M. Cazzanelli, M. Orlandi, A. Miotello, L. Fiori, Hydrothermal carbonization of glucose: secondary char properties, reaction pathways, and kinetics, Chem. Eng. J. 449 (2022), https://doi.org/10.1016/j.cej.2022.137827.

[18] P. Stutzenstein, B. Weiner, R. Köhler, C. Pfeifer, F.-D. Kopinke, Wet oxidation of process water from hydrothermal carbonization of biomass with nitrate as oxidant, Chem. Eng. J. 339 (2018) 1–6, https://doi.org/10.1016/j.cej.2018.01.080.

[19] M. Gürü, A.Y. Bilgesü, V. Pamuk, Production of oxalic acid from sugar beet molasses by formed nitrogen oxides, Bioresour. Technol. 77 (2001) 81–86, https://doi.org/10.1016/s0960-8524(00)00122-x.

[20] A. Sakthisabarimoorthi, S.A. Martin Britto Dhas, M. Jose, Fabrication of monodispersed α-Fe_2O_3@SiO_2 core-shell nanospheres and investigation of their

dielectric behavior, J. Alloys Compd. 771 (2019) 1–8, https://doi.org/10.1016/j.jallcom.2018.08.250.
[21] G. Jin, Q. Zhou, Z. Duan, K. Shen, Z. Dong, S. Deng, P. Yang, Multistage template-oriented design and tailoring of the hierarchical porous biocarbon materials for high-performance supercapacitors, ACS Omega 9 (2024) 47557–47566, https://doi.org/10.1021/acsomega.4c06494.
[22] S. Seo, I. Jeon, R. Xiang, C. Lee, H. Zhang, T. Tanaka, J.-W. Lee, D. Suh, T. Ogamoto, R. Nishikubo, A. Saeki, S. Chiashi, J. Shiomi, H. Kataura, H.M. Lee, Y. Yang, Y. Matsuo, S. Maruyama, Semiconducting carbon nanotubes as crystal growth templates and grain bridges in perovskite solar cells, J Mater Chem A 7 (2019) 12987–12992, https://doi.org/10.1039/c9ta02629k.
[23] F. Yan, C. Gao, S. Peng, X. Yang, Z. Li, M. Yang, T. Zeng, Y. Yang, Insights of physicochemical structure changes of bituminous coal with acidification-assisted controlled electric pulse through SEM, XRD and FTIR, Gas Sci. Eng. 132 (2024), https://doi.org/10.1016/j.jgsce.2024.205496.
[24] X. Niu, Y. Feng, Y. Xu, W. Yang, Synthesis of hollow Al-doped MgO spheres via a sacrificial templating method for enhanced CO_2 adsorption, J. Nat. Gas Sci. Eng. 88 (2021), https://doi.org/10.1016/j.jngse.2021.103814.
[25] H. Han, F. Huang, F. Wang, H. Cai, X. Qin, Y. Xu, Preparation and photocatalytic performance of ZnO/carbon composites for organic dyes degradation, App. Phys. A 129 (2023), https://doi.org/10.1007/s00339-023-06965-8.
[26] M.K. Naskar, Soft solution processing for the synthesis of alumina nanoparticles in the presence of glucose, J. Am. Ceram. Soc. 93 (2010) 1260–1263, https://doi.org/10.1111/j.1551-2916.2009.03555.x.
[27] B. Liu, L. Li, L. Qu, Preparation of multi cage-like zinc oxide Nanopowder with high specific surface area via a large-scale hydrothermal method, Adv. Mater. Res. 476-478 (2012) 714–720, https://doi.org/10.4028/www.scientific.net/AMR.476-478.714.
[28] S. Basavaraja, D.S. Balaji, M.D. Bedre, D. Raghunandan, P.M. Prithviraj Swamy, A. Venkataraman, Solvothermal synthesis and characterization of acicular α-Fe_2O_3 nanoparticles, Bull. Mater. Sci. 34 (2012) 1313–1317, https://doi.org/10.1007/s12034-011-0321-z.
[29] G.S. Li, R.L. Smith, H. Inomata, K. Arai, Preparation and magnetization of hematite nanocrystals with amorphous iron oxide layers by hydrothermal conditions, Bull. Mater. Sci. 37 (2002) 949–955, https://doi.org/10.1016/s0025-5408(02)00695-5.
[30] V. Jagadeesha Angadi, S. Kubrin, M.A. Sayed, A. Kumar, K. Sharma, M. Shkir, S. O. Manjunatha, R.A.P. Ribeiro, M.C. Oliveira, E. Longo, N. Basavegowda, Structural and magnetic modulations in α-Fe_2O_3 ceramic nanoparticles: a multifaceted study with DFT calculations, Ceram. Int. (2025), https://doi.org/10.1016/j.ceramint.2025.05.073.
[31] J.C. Souza, R.A.P. Ribeiro, L.G. da Trindade, R.C.D. Oliveira, L.D. Costa, M.C. De Oliveira, S.R. De Lazaro, J.R. Sambrano, C.R. Mendonça, L. de Boni, F.M.L. Pontes, A.J.A. De Oliveira, E.R. Leite, E. Longo, Unconventional disorder by femtosecond laser irradiation in Fe_2O_3, ACS, Omega 6 (2021) 28049–28062, https://doi.org/10.1021/acsomega.1c04079.
[32] L.-L. Tian, M.-J. Zhang, C. Wu, Y. Wei, J.-X. Zheng, L.-P. Lin, J. Lu, K. Amine, Q.-C. Zhuang, F. Pan, Γ-Fe_2O_3 Nanocrystalline microspheres with hybrid behavior of battery-supercapacitor for superior Lithium storage, ACS Appl. Mater. Interfaces 7 (2015) 26284–26290, https://doi.org/10.1021/acsami.5b08756.
[33] W. Lu, L. Yan, W. Ye, J. Ning, Y. Zhong, Y. Hu, Defect engineering of electrode materials towards superior reaction kinetics for high-performance supercapacitors, J Mater Chem A 10 (2022) 15267–15296, https://doi.org/10.1039/d2ta02930h.
[34] F. Sarf, I. Karaduman Er, E. Yakar, S. Acar, The influence of annealing temperature on the gas sensing properties of multifunctional hematite (α-Fe_2O_3) films, J. Mater. Sci. Mater. Electron. 36 (2025), https://doi.org/10.1007/s10854-025-14244-w.
[35] X. Ding, J. Jin, X. Huang, S. Zhou, A. Xiao, Y. Chen, C. Zuo, An in situ template for the synthesis of tunable hollow carbon particles for high-performance lithium–sulfur batteries, ACS Omega 4 (2019) 16088–16094, https://doi.org/10.1021/acsomega.9b02287.
[36] M. Sevilla, A.B. Fuertes, Chemical and structural properties of carbonaceous products obtained by hydrothermal carbonization of saccharides, Chem. Eur. J. 15 (2009) 4195–4203, https://doi.org/10.1002/chem.200802097.
[37] J. Jia, R. Wang, H. Chen, H. Liu, Q. Xue, Q. Yin, Z. Zhao, Interaction mechanism between cellulose and hemicellulose during the hydrothermal carbonization of lignocellulosic biomass, Energy Sci. Eng. 10 (2022) 2076–2087, https://doi.org/10.1002/ese3.1117.
[38] M. Li, W. Li, S. Liu, Control of the morphology and chemical properties of carbon spheres prepared from glucose by a hydrothermal method, J. Mater. Res. 27 (2012) 1117–1123, https://doi.org/10.1557/jmr.2011.447.
[39] Y. Luo, T. Lu, S. Jin, K. Ye, S. Yu, X. Zhang, X. Wu, P. Ma, J.W. Tester, K. Wang, Elucidating the intrinsic core-shell structure of carbon nanospheres from glucose hydrothermal carbonization, J. Supercrit. Fluids 210 (2024), https://doi.org/10.1016/j.supflu.2024.106290.
[40] D. Lin-Vien, The Handbook of Infrared and Raman Characteristic Frequencies of Organic Molecules, 1991.
[41] Y. Qi, M. Zhang, L. Qi, Y. Qi, Mechanism for the formation and growth of carbonaceous spheres from sucrose by hydrothermal carbonization, RSC Adv. 6 (2016) 20814–20823, https://doi.org/10.1039/C5RA26725K.
[42] S. Weng, Y. Xu, Fourier Transform Infrared Spectrum Analysis, 2016.
[43] L. Qiao, J. Chen, L.Q. Jiang, J.W. Zheng, The pH influence on the preparation of hollow Fe_2O_3 spheres by hydrothermal method, Adv. Mater. Res. 669 (2013) 119–123, https://doi.org/10.4028/www.scientific.net/AMR.669.119.
[44] Q.Z. Zeng, S.Y. Ma, W.X. Jin, H.M. Yang, H. Chen, Q. Ge, L. Ma, Hydrothermal synthesis of monodisperse α-Fe_2O_3 hollow microspheroids and their high gas-sensing properties, J. Alloys Compd. 705 (2017) 427–437, https://doi.org/10.1016/j.jallcom.2017.01.268.
[45] C. Wang, P. Sireesha, J. Shang, J.S. McCloy, J. Liu, W.-H. Zhong, Converting commercial Fe_2O_3 to effective anode material using glucose as “etching” agent, Ceram. Int. 49 (2023) 32652–32662, https://doi.org/10.1016/j.ceramint.2023.07.234.
[46] M. Li, W. Li, S. Liu, Hydrothermal synthesis, characterization, and KOH activation of carbon spheres from glucose, Carbohydr. Res. 346 (2011) 999–1004, https://doi.org/10.1016/j.carres.2011.03.020.
[47] B. Liu, X. Hu, Hollow Micro- and nanomaterials: synthesis and applications, advanced nanomaterials for pollutant sensing and environmental, Catalysis (2020) 1–38.
[48] D.B.K. Chu, J.S. Owen, B. Peters, Nucleation and growth kinetics from LaMer burst data, J. Phys. Chem. A 121 (2017) 7511–7517, https://doi.org/10.1021/acs.jpca.7b08368.
[49] M. Thommes, K. Kaneko, A.V. Neimark, J.P. Olivier, F. Rodriguez-Reinoso, J. Rouquerol, K.S.W. Sing, Physisorption of gases, with special reference to the evaluation of surface area and pore size distribution (IUPAC technical report), Pure Appl. Chem. 87 (2015) 1051–1069, https://doi.org/10.1515/pac-2014-1117.
[50] Y. Guo, Q. Liu, X. Tang, H. Liang, G. Li, L. Yang, L. Wang, X. Li, Y. Sun, Photocatalytic membrane coated with α-Fe_2O_3/Fe_3O_4 for enhanced filtration performance and antifouling property in surface water treatment, Chemosphere 341 (2023), https://doi.org/10.1016/j.chemosphere.2023.140114.
[51] T. Yamashita, P. Hayes, Analysis of XPS spectra of Fe^{2+} and Fe^{3+} ions in oxide materials, Appl. Surf. Sci. 254 (2008) 2441–2449, https://doi.org/10.1016/j.apsusc.2007.09.063.
[52] X. Qiao, J. Huang, Nanoneedle-assembled hollow α-Fe_2O_3 microflowers as Li-ion battery anode with high capacity and good temperature tolerance, J. Electroanal. Chem. 898 (2021), https://doi.org/10.1016/j.jelechem.2021.115625.
[53] A. Magomedova, A. Isaev, F. Orudzhev, Oxygen vacancies enhanced photo-Fenton-like catalytic degradation of rhodamine B by electrochemical synthesized α-Fe_2O_3 nanoparticles, Inorg. Chem. Commun. 165 (2024), https://doi.org/10.1016/j.inoche.2024.112563.
[54] A.M. Tamboli, M.S. Tamboli, S.K. Shinde, J. Byeon, N.T.N. Truong, C. Kim, C. Park, Uniform and fully decorated novel Li-doped α-Fe_2O_3 nanoparticles for high performance supercapacitors, J. Alloy. Compds. 928 (2022), https://doi.org/10.1016/j.jallcom.2022.167242.
[55] C. Zhang, S. Liu, T. Chen, Z. Li, J. Hao, Oxygen vacancy-engineered Fe_2O_3 nanocubes via a task-specific ionic liquid for electrocatalytic N_2 fixation, Chem. Commun. 55 (2019) 7370–7373, https://doi.org/10.1039/c9cc03221e.
[56] L. Gao, C. Tang, J. Liu, L. He, H. Wang, Z. Ke, W. Li, C. Jiang, D. He, L. Cheng, X. Xiao, Oxygen vacancy-induced Electron density tuning of Fe_3O_4 for enhanced oxygen evolution catalysis, Energy Environ. Mater. 4 (2020) 392–398, https://doi.org/10.1002/eem2.12112.
[57] S. Liu, X. Zhang, N. Wang, N. Karimov, Y. Wang, Z. Gao, D. Wang, B. Zhu, S. Gao, F. Yang, Modulating d-band center of iron oxide via interfacial oxygen vacancies engineering for boosting electrocatalytic nitrogen reduction, Mol. Catal. 578 (2025), https://doi.org/10.1016/j.mcat.2025.115031.
[58] X. Liang, L. Wang, T. Wen, H. Liu, J. Zhang, Z. Liu, C. Zhu, C. Long, Mesoporous poorly crystalline α-Fe_2O_3 with abundant oxygen vacancies and acid sites for ozone decomposition, Sci. Total Environ. 804 (2022), https://doi.org/10.1016/j.scitotenv.2021.150161.
[59] M.-M. Titirici, M. Antonietti, A. Thomas, A generalized synthesis of metal oxide hollow spheres using a hydrothermal approach, Chem. Mater. 18 (2006) 3808–3812, https://doi.org/10.1021/cm052768u.